Article

Physicochemical Characterization of Clay and Study of Cationic Methylene Blue Dye Adsorption

Zineb El Kerdoudi, Jaouad Bensalah,* Nouhaila Ferraa, Abdelali El Mekkaoui, Avni Berisha, Zaki Safi, Hanae Ouaddari, Farid Khallouki, Musaab Dauelbait,* Hiba-Allah Nafidi, Abdel-Rhman Z. Gaafar, Mohammed Bourhia, Amar Habsaoui, and Nouredine EL Mejdoub

Read Online

ACCESS | Metrics & More | Article Recommendations

ABSTRACT: In an attempt to examine novel adsorbents in accessing an ideal adsorption system, this study aimed to help understand the main and secondary characteristics of a Moroccan natural clay. X-ray fluorescence, infrared, and scanning electron microscopy with energy-dispersive X-ray spectroscopy analysis (SEM-EDX) were used for the identification. The findings demonstrate that this Clay is composed of a mixture of quartz, calcite, magnetite, and Rutile in very high proportions. SEM revealed the presence of clay grains in the presence of fine particles and irregularly contoured sticks. The results of semiquantitative detection by EDX also reveal the presence of certain mineral species (Si, Al, Mg, Fe, K, Cl, S, Ca, and Na). The exploited kinetic technique was achieved using two different kinetic models: first- and second-order rate laws. Commensurate to the obtained results, the 2-sec order model better described the adsorption of dye MB onto the natural clay. The results confirmed that the adsorption process followed the Langmuir model with the high coefficient correlation obtained which are very close to 1. In the sequel, DFT results revealed that the HOMO and LUMO surfaces of the methylene blue dye are mostly distributed on all dye parts, reflecting possible strong interactions with the clay. The quantum descriptors investigated in this study identify the most nucleophilic and electrophilic centers that can be used to suggest a suitable mechanism for the adsorption of the dye by the clay. The values of enthalpy ΔH^0 and entropy ΔS^0 of activation were -15.88 kJ mol^{-1} and -0.021 J mol^{-1} K^{-1}, respectively, show that the nature of the adsorption process of MB on clay is exothermic and the order of distribution of the dye molecules on the adsorbent increases with respect to that of the solution so the negative values of ΔG^0 (from -9.62 to -8.99 kJ mol^{-1}) indicate that the adsorption process is spontaneous.
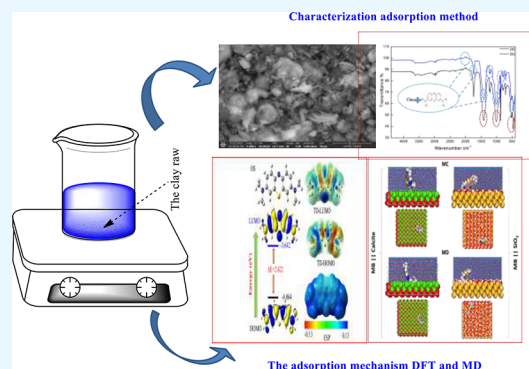
1. INTRODUCTION

Most dyes are commonly used in the printing, food design, cosmetics, and clinical fields, but more particularly in the textile field for their stability and ease of manufacture, or their variety of colors.[1] However, these coloring substances are a source of environmental pollution and are dangerous for certain organisms due to their persistence, toxicity, and mutagenic and carcinogenic properties. Therefore, the need to reduce the environmental impacts of pollutants, such as the popular cationic dyes, is imperative.[2]

Physico-chemical methods exploited to remove dyes from micropollutants include photochemical degradation, membrane separation, reverse osmosis, coagulation, oxidation as well as adsorption. Adsorption is one of the best techniques used to remove pollution from effluents.[3] Research to find more economical and better-known adsorbents remains very important. Indeed, from this perspective, the possibility of choosing clays as an adsorption medium is very interesting due

to their important role in certain fields, such as the manufacture of drugs and the treatment of polluted waters.[4]

The present work investigated the removal of the cationic methylene blue dye by a clay originating from the GHARB region (KHENICHET-Sidi Kacem-Morocco). Methylene blue is a cationic dye and has three cyclic rings and one S atom. The high sorption affinity of the cationic/basic methylene blue dye by many adsorbents has been already reported in the literature.[5]

The adsorbent with a particle size equal to or less than 56 μm is used in its natural state without initial treatment. Various parameters were studied including temperature, the quantity of
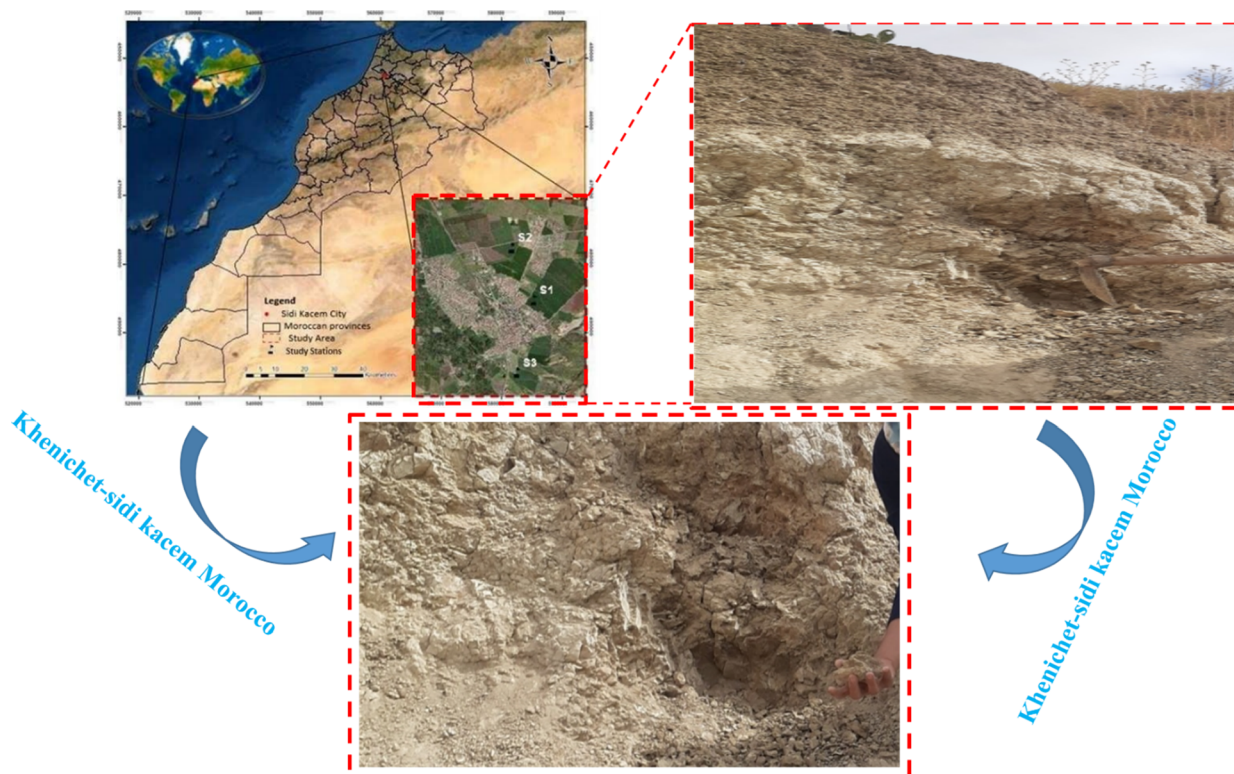
Figure 1. Images of the clay raw Khenichet-Sidi Kacem operational to date.

adsorbent, the initial dye concentration, as well as the pH. The study aimed to determine the adsorption kinetics of organic methylene blue cationic dye onto the surface morphology of clay particles while investigating the impact of dye concentration and particle size on the adsorption kinetics as well as the adsorption isotherm.[6]

2. MATERIALS AND METHODS

2.1. Preparation Adsorbent. In this work, we used raw clay located near Oued Ouergha, in Khenichet, northwest Morocco. Its geographic coordinates in decimal format: latitude, 34.4403282, longitude −5.6852428. This gives, after conversion into degrees, minutes, and seconds, these coordinates: 34°26′25.18 north latitude, −5°41′6.87 west longitude. Collected samples are ground and sieved to a size of 56 μm or less, then dried at 105 °C for 24 h, and stored in a dry place until use (Figure 1).

2.2. Preparation of the Solution. MB stock solution was prepared by dissolving a sufficient amount of MB in distilled water. The solutions used in the tests were obtained by dissolving the latter (stock solution) in distilled water to reach the desired concentration. Their starting pH was adjusted with a HCl-based or NaOH-based solution.

2.3. Experimental Section. *2.3.1. Adsorption Kinetic.* Adsorption tests were performed in series at different starting values of pH, temperature, and dye concentration.[7] These methylene blue dye adsorption experiments were performed by adding a specific dose of clay to a 100 mL volume of methylene blue organic dye solution at a concentration of 10 mg L^{-1}. For 3 h (adsorption's duration), the samples were taken in a 5, 10, and then 30 min time lapse for this duration. To separate this colored solution from the adsorbent, it was centrifuged at 3000 rpm for 5 min and the absorbance was measured by UV spectroscopy at a wavelength (λ_{max} = 665 nm). A

spectrophotometer UV−visible of the type "Zuzispectrophotometer 4201/50" was used.

2.3.2. UV/Visible Spectrophotometer. The absorption value of the colored water was determined using a spectrometer UV/visible at λ_{max} = 665.00 nm.

The dye concentration is measured using curve calibration performed with a range of known MB concentrations of dye. The capacity adsorption of the methylene blue colorant with clay has been calculated utilizing the following formula eq 1:

$$Q_t = \frac{(C_0 - C_t)V}{m} \tag{1}$$

C_0, C_t are, respectively, the initial and equilibrium concentrations.

m: Mass of clay.

V: Volume corresponded to the methylene blue dye.

2.4. Modeling of Equilibrium and Kinetic. The simulation of the experimental isotherm data was performed using ORIGIN software (version 2018). The choice of the most relevant model(s) for understanding the MB adsorption process onto the Cs material depended on the values and correlation coefficient R^2 given in all tables present in the current work.

2.5. DFT Details. Geometries of the methylene blue (MB) in the ground states were optimized using the hybrid (DFT/B3LYP) method in coupling with the 6-311+G(d,p) basis set. The optimization process was carried out in an aqueous solution using the polarized continuum model of solvation (PCM).[8] Frequency calculations were also performed at the same level of theory to ensure that the structure is minimum to the potential energy surface with no imaginary frequencies. All calculations were employed using the Gaussian 16 program package. The energies of the highest occupied and lowest unoccupied molecular orbitals (E_H and E_L) were extracted by

visualizing the output file using the Gauss view program.[9] The E_H and E_L values were used to calculate the energy gap ($\Delta E = E_L - E_H$) of the MB. In order to calculate the chemical reactivity descriptors for MB, the vertical ionization potential (IP_v) and vertical electron affinity (EA_v) were calculated using eq 2:

$$IP_v = E_0^{\pm E_0 \wedge EA_v = E_0^{-} - E_0}$$ (2)

where E_0 is the total energy of the optimized structure and E_0^+ and E_0^- are the energies of the cationic radical and anionic radical at the optimized structure of the neutral species, respectively. The chemical reactivity descriptors such as absolute electronegativity (χ), global hardness (η), softness (σ), electrophilicity (ω), global nucleophilicity (N), and electronic effect of feedback (back-donation), followed by the electronic energy (ΔE_{b-d}), were calculated using the following eqs 3 and 4:[10]

$$\chi = \frac{VIP + VEA}{2}, \ \eta = \frac{VIP - VEA}{2}, \ S = \frac{1}{\eta}, \ \omega = \frac{\chi^2}{2\eta},$$
$$\Delta E_{b-d} = \frac{-\eta}{4}, \ \wedge$$ (3)

$$N = E_H^{MB} - E_H^{TCE}$$ (4)

where E_H^{MB} and E_H^{TCE} are the energies of the highest occupied molecular orbitals of MB and tetracyanoethylene (TCE), which is used as a nucleophilicity reference. In the current study, $E_H^{TCE} = -9.07398$ eV is taken as obtained using the same level of theory. The results of the chemical reactivity descriptor are summarized in Table 9.

2.6. Monte Carlo (MC) and Molecular Dynamic (MD). To study the intricate interplay between MB molecules and the simulated clay surface, MC simulations have proven to be indispensable to complement experimental approaches. The computational calculations encompassed two distinct surface types: (1) SiO_2-OH[11] (packed with 1 MB and 1800 water molecules) and (2) calcite (packed with 1 MB and 2500 water molecules).[12,13] These simulations facilitated a comprehensive exploration of the molecular dynamics[12,13] and binding characteristics of MB on both surface models, shedding light on the intricate nature of the interactions and paving the way for an enhanced understanding of MB adsorption mechanisms on clay surfaces.[11]

By employing the Bravais−Friedel−Donnay Harker (BFDH) crystal morphology calculation,[11] the most stable structure of the surfaces was determined through rigorous calculations. This approach ensured accuracy in depicting the surface's arrangement, thus providing a reliable foundation for further investigations and analysis of its properties and behaviors. Both the SiO_2-OH and calcite surface models were under periodic boundary conditions with the size of (1) $SiO_2-OH \parallel 39.304 \times 43.2416 \times 8.509 \ \text{Å}^3 \parallel$ and (2) calcite $\parallel 51.008 \times 39.920 \times 6.772 \ \text{Å}^3 \parallel$ with an inclusion of 20 Å vacuum layer to accommodate the simulated media. The MC and MD calculations of the simulation employed the widely utilized COMPASS III force field, known for its versatility and reliability.[11,14] MD simulations were executed under the NVT ensemble at a temperature of 298 K, ensuring the system's stability and mimicking real-world conditions. The MD simulation spanned a total duration of 0.8 ns, allowing for a detailed exploration of the molecular dynamics and inter-actions within the system over a significant time frame.[15]

These calculations facilitated a comprehensive understanding of the system's behavior and properties under the given conditions.[16]

2.7. Data Modeling. *2.7.1. Pseudo-First-Order and Pseudo-Second-Order.* Pseudo first order theory of kinetics is more suitable when the concentration of solutes is low.

The pseudo first order is given by eq 5.

$$\log(Q_e - Q_t) = \log(Q_e) - K_1 t$$ (5)

The pseudo-second-order kinetic model describes the adsorption of the adsorbate onto adsorbents based on equilibrium adsorption. The reaction rate of this pseudo-second-order depends on the quantity of adsorbed solute as well as on the quantity of equilibrium adsorbed.

The kinetics using of the adsorption process is described by the following eq 6.[17]

$$\frac{t}{Q_t} = \left[\frac{1}{K_2 Q_e^2}\right] + \frac{1}{Q_e} t$$ (6)

Q_e: The amount of dye adsorbed at equilibrium (mg g^{-1}).
Q_t: The amount of dye adsorbed at any time t (mg g^{-1}).
K_1: The constant of speed (min^{-1}).
K_2: The constant pseudo-2^{sec}-order (g mg^{-1} min^{-1}).

2.7.2. Langmuir Isotherm. Langmuir's model is based on the following hypotheses:

Formation of only one adsorbate coating on the adsorbent surface.

Existence of certain sites of adsorption.

The uniform surface with the absence of any interaction between adsorbed molecules

Langmuir's equation is written as follows (eq 7).

$$\frac{C_e}{Q_e} = \frac{C_e}{Q_m} + \frac{1}{(K_L \cdot Q_m)}$$ (7)

where

C_e: Concentration Equilibrium present in the adsorbent study (mg L^{-1}).
Q_e: Equilibrium adsorbed amount per gram of the adsorbent present (mg g^{-1}).
Q_0: Maximum adsorption capacity (mg g^{-1}).
K_L: Equilibrium constant.

The main characteristics of the isotherm Langmuir are expressed as a function of the scale-free separation coefficient R_L which is expressed as follows (8).[18]

$$R_L = \frac{1}{1 + K_L C_0}$$ (8)

where

C_0: The first concentration (mg L^{-1}).
K_L: The constant of Langmuir (L mg^{-1}).
R_L: Indicates Langmuir's isotherm shape.
If
$R_L > 1$ shows unfavorable adsorption.
$R_L = 1$ shows a linear adsorption.
$0 < R_L < 1$ shows favorable adsorption.
$R_L = 0$ shows irreversible adsorption.

2.7.3. Freundlich Isotherm. Freundlich isotherm considers a multilayer absorption with a heterogeneous surface of the adsorbent. Freundlich equation is given as follows (eq 9).[19]
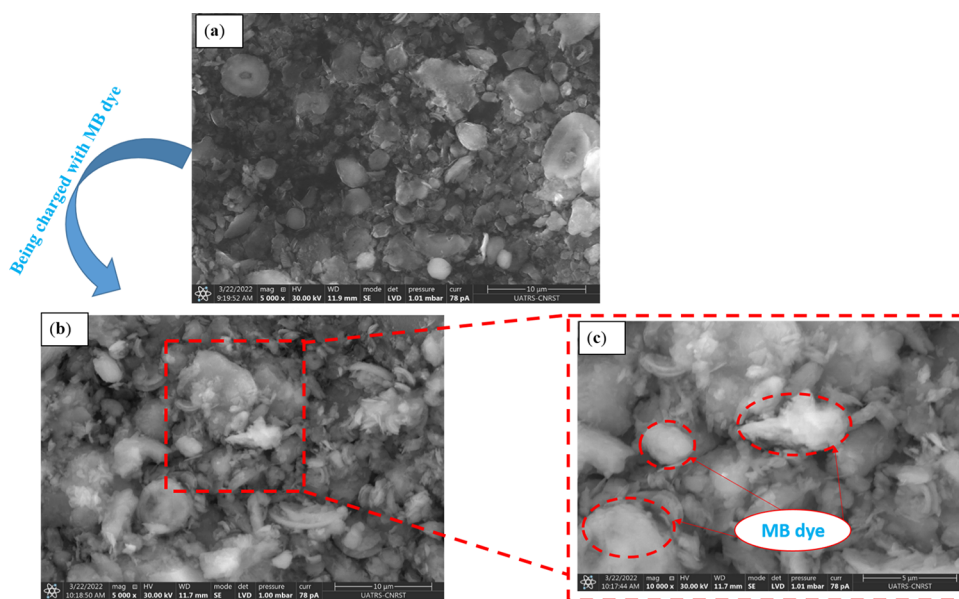
Figure 2. Clay SEM observation before adsorption (a), (b) and (c) after MB adsorption.

$$\log Q_e = \log K_F + \frac{1}{n}\log C_e \tag{9}$$

where

Q_e: Quantity absorbed by gram of adsorbent (mg g^{-1}).

C_e: Concentration of the solutions at equilibrium (mg L^{-1})

K_F and $1/n$: Constants respectively associated of Freundlich study with the adsorption capacity (l/g) and the adsorption affinity

2.7.4. Themodynamic Studies. The parameters such as free energy ($\Delta G°$), enthalpy change ($\Delta H°$), and entropy change ($\Delta S°$) can be estimated from the equilibrium constants at different temperatures.

The enthalpy ($\Delta H°$), entropy ($\Delta S°$), and the free energy change of the adsorption reaction were represented following the respective eqs 10 and 11:[20]

$$\ln(K_L) = \frac{\Delta S}{R} - \frac{\Delta H}{RT} \tag{10}$$

$$\Delta G = \Delta H - T\Delta S \tag{11}$$

2.8. Characterization Method. *2.8.1. X-ray Diffraction.* X-ray diffraction is a powerful technique for studying crystals in the solid state. It gives access to their crystalline structure. It is indispensable for identifying the clay minerals in natural clays as well as the associated minerals ("impurities").

X-ray diffractometric analyses were performed using X'Pert3 Powder "PAN analytical" to identify the predominant phases of the clay mineral.

The crystallinity of the clay natural was investigated by X-ray diffraction (XRD) analysis, using a powder X-ray diffractometer (D8 Advance A25 Bruker AXS GbmH., Germany) with Cu Kα radiation at 40 kV and 25 mA, in the range of $2\theta = 5-100°$ at a scanning rate of $0.02°$ s^{-1}. The various crystallinity (CrI) index was according to calculation to the Segal eq 12:[21]

$$\text{CrI} = 100 \times (I_{200} - I_{am})/I_{200} \tag{12}$$

where I_{200} is the intensity diffraction at $2\theta = 10-30°$ and I_{am} is the minimum intensity diffraction at $2\theta = 10-100°$.

The crystallite size was calculated as per the Scherrer eq 13

$$L_{h,k,l} = 0.94 \times \lambda\beta\cos(\theta) \tag{13}$$

where λ is the X-ray wavelength;

β is the full width at half-maximum in radians;

θ is the Bragg angle;

2.8.2. SEM−EDX. An electron microscope creates a high-resolution image at the micro- or nanoscale by using a focused incident electron beam to give an idea of the texture and morphology of a sample. Electron microscopes are capable of magnifications of up to 500,000 times. In this study, the electron microscope used was a FESEM quanta 250 equipped with an EDX detector. SEM images were used to determine the surface condition and morphology of native and pretreated biomass. SEM−EDX analyses were carried out using the QUATTRO S-FEG-Thermofisher scientific. A scanning electron microscope (Quanta 250 FEG, FEI, USA) with an accelerating voltage of 15 kV was used to study the microstructure and surface morphology of the cellulose microfibers obtained.[22]

2.8.3. Fourier Transform Infrared Spectroscopy. We use this technique to determine the presence or absence of organic matter in clay materials as well as the presence of carbonate groups.

To analyze the changes chemical of the samples and functional investigate groups using the extracted clay natural, we used Fourier transform infrared spectroscopy. The infrared spectra were recorded on a Cary 660 infrared spectrometer (Agilent Technologies, USA) in a wavelength range of 400−4000 cm^{-1} with a resolution of 4 cm^{-1} using.[23]

2.8.4. Fluorescence X. A chemical analysis was performed on the clay raw material using the PANalytical Epsilon 3 a benchtop energy dispersive X-ray fluorescence spectrometer.[24]

X-ray fluorescence spectrometry is an elementary analysis technique for determining the chemical species contained in a sample. The principle of this method is to bombard the material to be analyzed with a beam of X-rays, resulting in secondary X-ray emission. The result is a spectrum of emitted X-rays showing the characteristic peaks of the various elements present in the sample. The spectrum can be analyzed in two ways: wavelength-dispersive and energy-dispersive analysis.
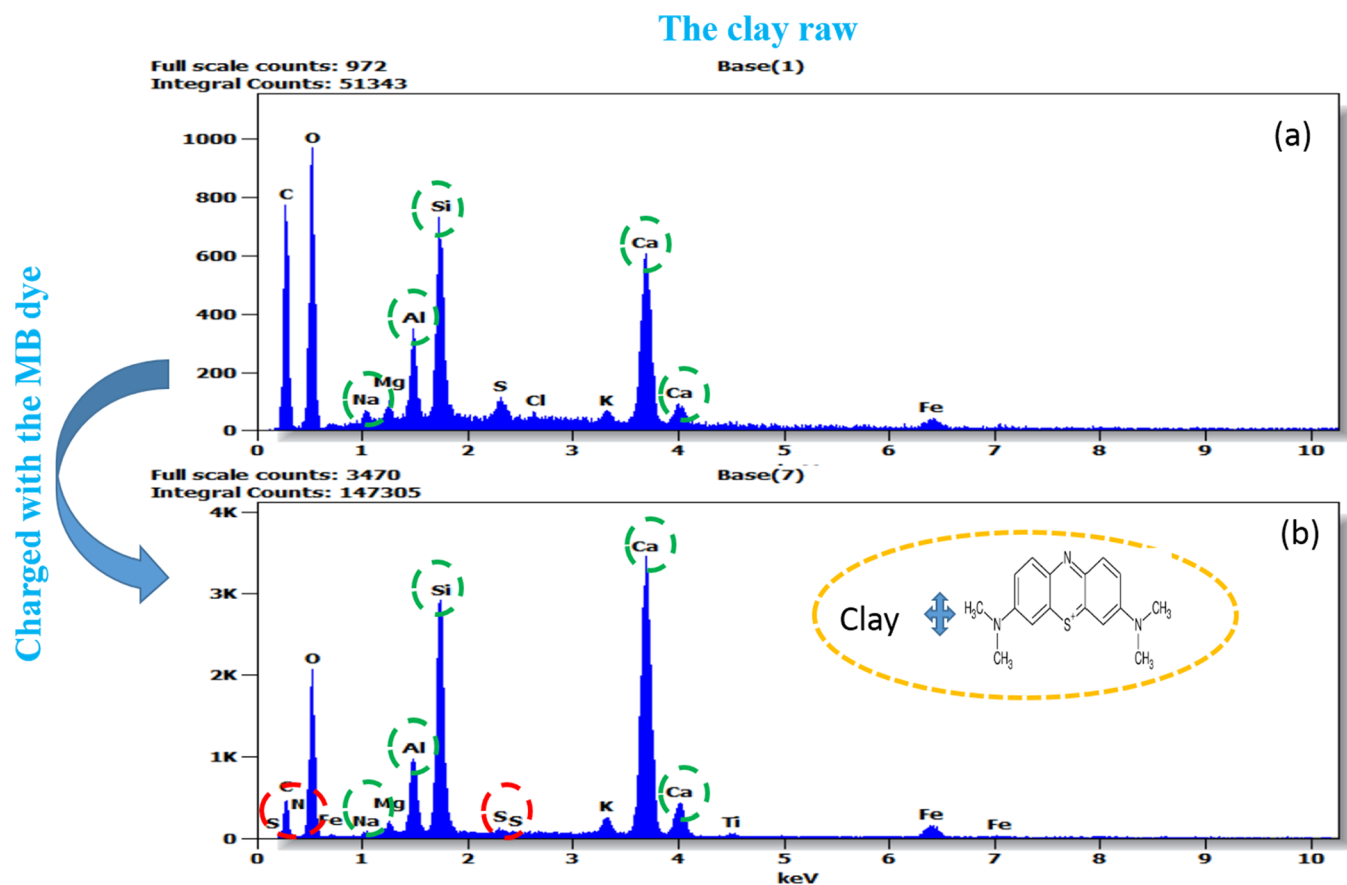
Figure 3. EDX of clay powder raw (a) and after MB adsorption (b).

The position of the peaks provides information about the nature of the element (qualitative analysis), while their intensity quantifies the content of each element.

In a fluorescence experiment using an interface and irrespective of the type of radiation incident, the fluorescence characteristic of the different species of interest is recorded as a function of the angle of incidence θ at which the impinges beam onto the interface. Here, species may denote either an element or a nuclide. X-rays induce fluorescence characteristics via ionization photoelectric of the various elements chemical.[25]

3. RESULTS AND DISCUSSION

3.1. Characterization. *3.1.1. Scanning Electron Microscopy/Energy Dispersive X-ray Spectroscopy.* Analytical microscopy (SEM) and energy dispersion X-ray spectrometry (EDX) were used to study the morphology of the clay surface and to qualitatively determine the elemental chemical composition (Figure 2).

SEM images of the clay, before and after MB molecules adsorbed are shown in Figure 2a,b, respectively. Figure 2c depicts an SEM micrograph of the adsorbent after MB dye adsorption.

The photographs obtained by SEM with different magnifications were taken on a fine powder of marly clay.

Clay micrographs (Figure 2a) demonstrated different surface magnifications of the clay raw material, which indicate a favorable multiphase structure for adsorbents, whereas Figure 2b shows that new phases were created because of MB adsorption.

From the EDX graph (Figure 3a), the presence of peaks of Ca, Si, and Al that initially exist in the clay is revealed. The spectrum obtained after charge of the MB polymeric on clay (Figure 3b) indicates one peak that represents the Cl^- ion of the MB dye as a result of the complex reaction.

3.1.2. FT-IR Spectroscopy. To help characterize the raw clay mineral, Fourier transforms of IR spectra are increasingly being increasingly used. The FTIR spectra are merged in Figure 4.
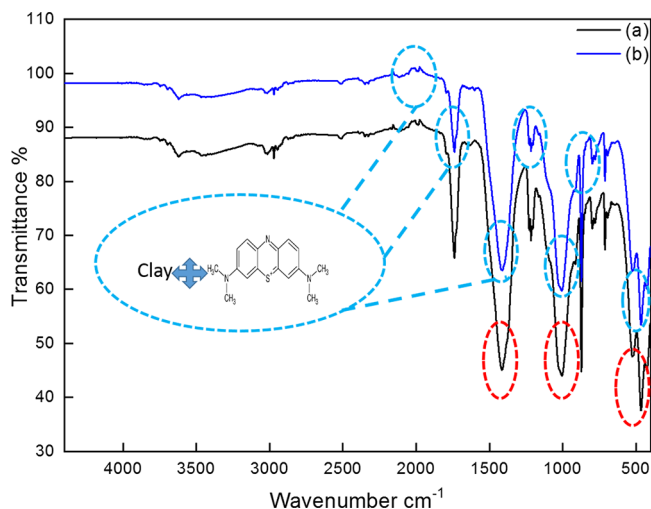

Figure 4. IR spectrum from clay raw (a), without treatment and charged with MB (b).

Figure 5. X-ray diffraction spectra of the raw clay (K: kaolinite, Q: quartz, I: Illite).

Fourier Transform Infrared Spectroscopy (FTIR) analyses were done to identify the functional groups and the molecular structure present in the clay raw without treatment and charged with MB. The spectrum range of FTIR was within 4500−400 cm⁻¹. The IR spectra (Figure 4) showed a band located at 3430.06 cm-1 wich refers to the vibrations elongation of Si−OH group,[26] the wide band at 1700.00 cm⁻¹ is attributed to C═O deformation. The absorption bands at 3430 and 1700 cm-1 are ascribed to − OH stretching vibration in physisorbed water.[27]

A band at 1004.99 788.00 and 696.00 cm⁻¹, was assigned to elongation vibrations of Si−O.[20] Two different bands at 867.29 and 713.25 cm⁻¹, indicate respectively the presence of Si−O− Al and Ca−C═O.[28] A band 794.14 cm⁻¹ corresponds to quartz, there is the bands characteristic of constitutive water that show up about 3000.00 cm⁻¹ʼ and two vibrational bands around 3624.61 and 3446.47 cm⁻¹ corresponding to the Al− OH-Al elongation.[29]

3.1.3. X-ray Diffraction. XRD diagrams identify the different minerals that make up the raw clay (Figure 5).

A study of the different compositions of this clay sample was characterized further by X-ray fluorescence analysis, and the results are presented (Table 1). Calcium (Ca), alumina (Al), silica (Si), and magnesium oxides (Mg−O) present were the main higher constituents of the used clay.[30]

As confirmed by the XRD fluorescence analysis, the predominant content of the SiO₂ is due to the presence of

Table 1. Identified Patterns List

score	compound name	scale factor	chemical structure
83.0	calcite	0.982	$Ca(CO_3)$
48.0	quartz	0.366	SiO_2
24.0	rutile, syn	0.035	TiO_2
13.0	magnetite	0.083	Fe_3O_4

quartz.[31] On the other hand, the presence of such a high content of Mg−O and Ca−O suggests that Mg^{2+} and Ca^{2+} are the predominant exchangeable cations.[32]

3.1.4. Fluorescence X. The raw clay was characterized by FX analysis, and the results of the study are summarized in Table 2.

Table 2. Clay Chemical Composition

constitute	concentration%	constitute	concentration %
SiO_2	25.46	MgO	0.05
Al_2O_3	07.65	MnO	0.01
CaO	29.54	Na_2O	0.30
Fe_2O_3	03.05	P_2O_5	0.39
K_2O	01.08	TiO_2	0.39
P-fire at 950 °C	27.31	total	96.28

From the table, we can see that loss on fire is defined as the mass loss of a raw grain powder passing through the furnace at 950 °C. In the case of our sample study, we find a value of 27.31%, which can be linked to the existence of carbonate and silicate minerals, and there is a very high percentage of silica and calcium oxide. This indicates the presence of calcium silicates $(CaSiO_3)$.[33]

3.2. Adsorption Studies. *3.2.1. Contact Time Effect.* The Kinetics of MB removal by raw clay was studied. The various results obtained are presented in (Figure 6). It can be seen that the adsorption kinetics is fast, the equilibrium time is reached after 20 min, then slowly reaches equilibrium with effective adsorption after an optimum adsorption time of 180 min.

From the curve obtained (Figure 6), it can be seen that this ability to remove the adsorbed MB dye increases with time. After 20 min, a level is reached, which corresponds to the saturation of the clay.

In this experiment, Q_m (MB) = 45.00 mg g⁻¹, is the maximum capacity studied. Maximum MB removal was
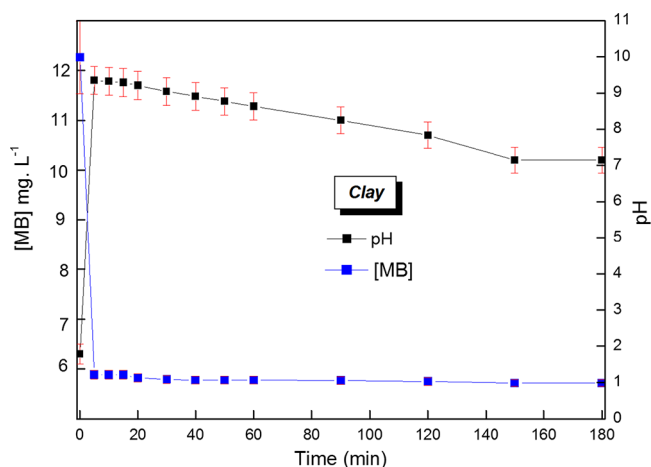
Figure 6. Variation of MB concentration and pH of colored water as a function of time.

observed at increasing pH values from 6.5 to 9.0 and then a slow decrease toward pH 7 because of the OH group found in natural clay.

3.2.2. Mass Effect. For estimating the best quantity of clay for the colored solution, the experiments have been done using 100 mL of the adsorbed cationic solution at 10 mg L^{-1} to which different quantities of clay from 0.015 to 2 g with pH = 6.5 and T = 25 °C have been added.

Figure 7 illustrates that the amount of dye adsorbed by the clay increases with the addition of the adsorbent up to a mass of 0.02 g, from which the bleaching efficiency hardly changes.
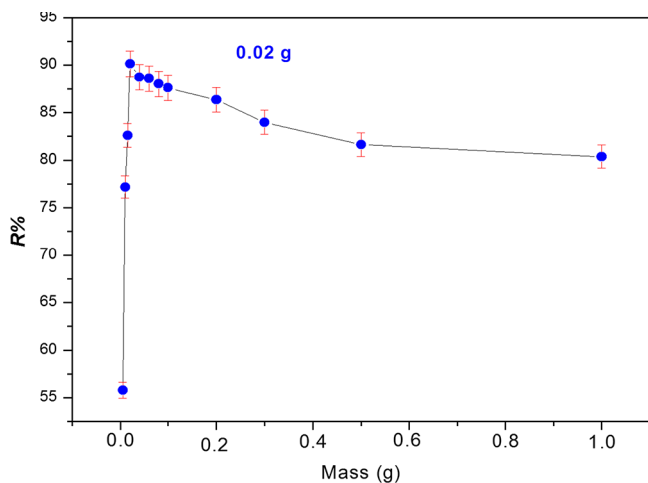
Figure 7. Variation present in the percentage of adsorption of methylene blue as a function of the quantity of raw clay.

This is because the adsorption sites increase with a low mass of the adsorbent and therefore decrease the methylene blue content with a fixed initial concentration.

The graph indicates a percent MB dye removal of 90.13% for a mass using 0.02 g of raw clay, and the value is chosen as the mass optimum for economic reasons.

These results revealed that the decrease in an adsorbent mass led to an increase in the number of active sites that could be obtained for the coordinate of the MB dye, consequently favoring the discoloration process of the solution aqueous studied.[34]

3.2.3. pH Effect. One very significant factor to consider in an adsorption study is the initial pH of the solution. This parameter's effect on the variation of adsorption capacity has been examined in a pH interval ranging from 2 to 12 (Figure 8), including around the normal pH (pH = 6.5).[34] The effect
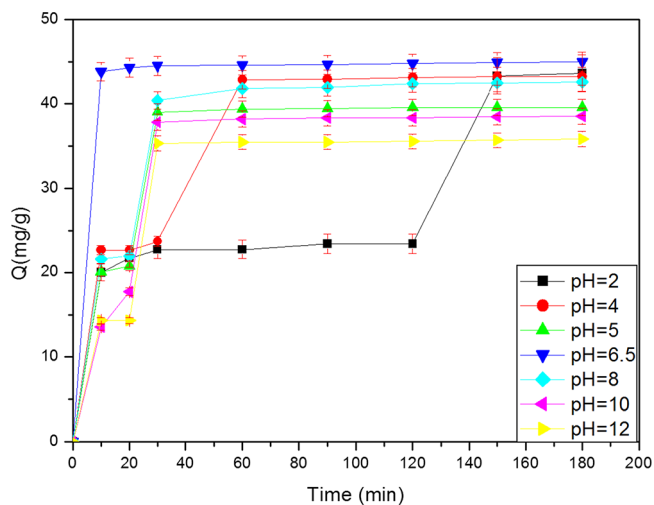
Figure 8. Evolution of the capacity adsorption of the MB as a function of time at different pH, m = 0.02 g, V = 100 mL, T = 25 °C, and [MB] = 10 mg L^{-1}.

of pH was assessed by preparing the adsorption curves. According to the experiments, 0.02 g of raw clay was added to 100 mL of the organic methylene blue cationic solution (10 mg L^{-1}) at room temperature (T = 25 °C).

The results presented in Figure 8 showed that, in general, the removal rate of dyes is very little influenced by pH variations (Table 3), and this is tuned by the basic character of the raw clay at room temperature (T = 25 °C).

Table 3. Variation in the Percent Removal of MB at Different pH

pH	2.0	4.0	5.0	6.5	8.0	10.0	12.0
R %	89.46	89.51	88.65	90.13	89.49	88.23	86.73

The tests showed that the pH of all MB solutions increased toward basic values. The MB solutions all change to basic after the inclusion of raw clay, so the effect of this parameter was neglected in this study.[34] The standard pH of the aqueous solution with no correction (pH 6.5) was assumed for the phenomenal adsorption tests in this study.

3.2.4. Temperature Effect. To evaluate the temperature-level effect on the ability to adsorb MB dye onto clay, 0.02 g was introduced into 100.0 mL of the MB dye, and then, adsorption of organic dye was performed at different temperatures ranging from 25 to 55 °C (Figure 9). The result of time of contact tests at different temperatures regarding the adsorption of MB on clay is shown (Figure 9).

Temperature was studied at 25, 35, 45, and 55 °C to determine the higher adsorption phenomenal rate of MB on clay; its variation modifies the equilibrium capacity.

The removal rate of MB by adsorption on clay decreases from 90.13 to 83.28% when the temperature is raised to a high level, showing adsorption as an *exothermic* process.
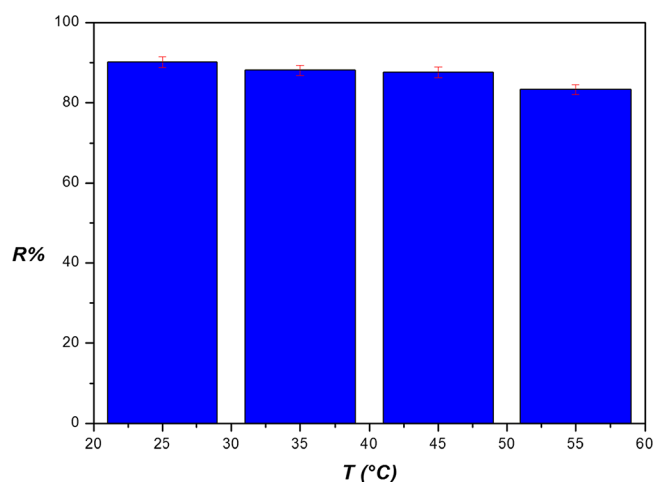
Figure 9. Variation of the MB removal percentage at different temperature values.

3.2.5. Concentration Effect. The plot of adsorption capacity versus contact time for different concentrations of Mb dye (10, 20, 40, 60, 80, 100, and 200 mg L^{-1}) are presented in Figure 10.
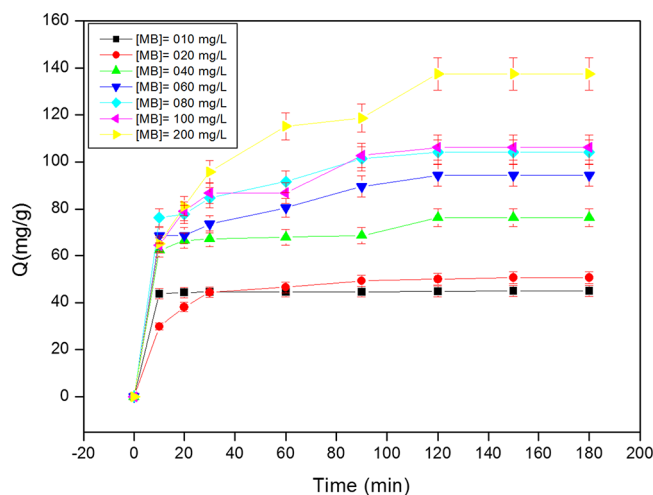

Figure 10. Evolution of MB dye adsorption at different concentrations as a function of time, (m_{clay} = 0.02 g, V = 100 mL, pH = 6.5, T = 25 °C).

The equilibrium time of 180 min was determined and was considered as the adsorption equilibrium time for all experiments.

We observed that the adsorption phenomenal process can be modeled into two processes:

- The initial process of fast adsorption takes place in 30 min.
- The second is a slow adsorption process between 30 and 180 min, with the increase in adsorption capacity being much slower than that of the first process.

Beyond 100 mg L^{-1} of MB dye, stabilization is obtained, which corresponds to a saturation of the clay (Q_{max} = 147. Two mg g^{-1}). One can interpret this phenomenon by the equilibrium of the existing active sites on the morphology surface of the clay.[34] The removal percent was found to be dependent on the initial concentration of the dye solution, and it is reported in Table 4.

The adsorption capacity changes from 45.00 to 147.20 mg g^{-1} for MB concentration of 10−200 mg L^{-1}, respectively. Dye removal, however, decreased from 90.13 to 14.70%.

3.3. Adsorption Kinetics Mechanism. The technical results of adsorption kinetics allowed us to obtain an appreciation of the mechanics of this phenomenal process as a function of the rate constant value.[34] Two models were applied to experimental results to study the behavior of the adsorption phenomenon of methylene blue on clay; both orders were tested; the results are depicted in Figures 11 and 12 and Tables 5 and 6.
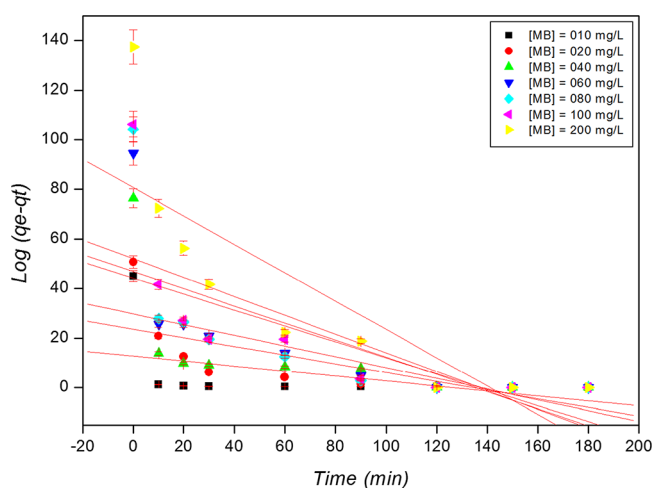

Figure 11. Kinetic model of the pseudo first order.

3.3.1. Pseudo First Order. 3.3.2. Pseudo Second Order. It should be noted that the best-fit plot was obtained when the data were used in testing the pseudo-second-order kinetic model. The calculated adsorption capacity (Q_{e-exp}) of 45.00 mg g^{-1} is very close to that measured experimentally, indicating that the methylene blue adsorption of the clay raw obeys the second pseudo order kinetics. As shown in Figure 11 and Table 5, the value of R^2 for the line of better fit is 0.79. The theoretical maximum adsorption capacity (Q_{e-cal}) is $10^{12.75}$ mg g^{-1} is very far from that of the experimentally obtained results (Q_{e-exp} is 45.00 mg g^{-1}), which corresponds to a kinetics of the second order. We can therefore conclude that chemisorption is the influx regulation step for the phenomenal process of MB on the morphology of the studied raw clay.

3.4. Isotherm Studies. Modeling of adsorption stability is to represent, via mathematical laws, the relationship at the stability of the quantity of pollutant in the liquid phase (C_e) and the adsorbed quantity on the material (Q_e).[35]

Table 4. Evolution of MB Retention Capacity on Raw Clay as a Function of Changing the MB Concentration

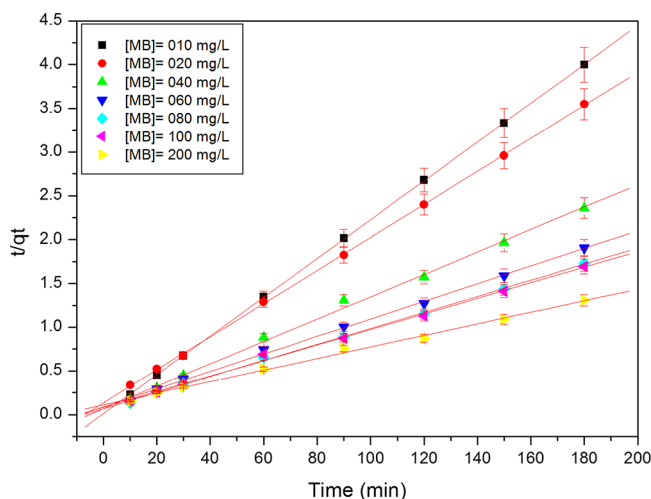| [MB] mg L^{-1}	10	20	40	60	80	100	200
Q_m (mg g^{-1})	45.00	58.35	92.35	107.65	131.95	145.85	147.20
R (%)	90.13	45.44	44.50	34.53	31.51	28.93	14.70

Figure 12. Kinetic model of the pseudo second order.

In our study, the Langmuir and Freundlich models adequately described for the study of adsorption isotherms of adsorbent/adsorbate systems were applied to analyze the adsorption equilibrium (Figures 13 and 15).

3.4.1. Langmuir. The fundamental characteristics of the Langmuir isotherm model can be expressed by the equilibrium dimensionless constant, R_L. The obtained R_L values showed favorable adsorption for the raw clays (Figure 14).

The curve presented in Figure 14 shows the factor separation values ranging from 0.10 to 0.20, which indicates that the adsorption process is favorable.

3.4.2. Freundlich. Table 7 shows the values of K_L, Q_0, K_F, and n, as well as the correlation coefficients.

The results illustrated in Table 7 indicate that the adsorption capacity of MB on clay depends on its porosity. We observed that the Langmuir isotherm has a higher R^2 correlation than the Freundlich isotherm for the studied clay;[36] this means that the Langmuir isotherm describes the adsorption much better than the Freundlich isotherm.

3.5. Thermodynamic Studies. Thermodynamic parameters showed the capacity and spontaneity of the adsorption phenomenon (Figure 16).

Table 8 defines the thermodynamic parameter values of $\Delta H°$, $\Delta S°$, and the free energy of the adsorption reaction $\Delta G°$.

We found that the values of enthalpy (ΔH) and entropy (ΔS) of activation were -3.25 kJ mol^{-1} and 10.39 J mol^{-1} K^{-1}, respectively.

Therefore, the negative value of (ΔH^0) and the positive value of (ΔS^0) showed the exothermic nature of the adsorption of MB on the clay, and the order of distribution of the dye molecules on the adsorbent increases compared to that of the solution. Finally, negative ΔG^0 values indicated that the adsorption process is spontaneous.[37]

3.6. Adsorption Mechanism DFT and MD. The possible interaction of the natural clay with the MB dye is illustrated in Figure 17. The adsorption phenomenon is governed by different factors, as exemplified by the functional activity and specificity of the MB dye molecule as well as the clay adsorbent morphology.

The organic dye adsorbent is a flat structure and can be easily adsorbed onto the clay due to van der Waals forces and heteroatomic interactions bonding. The strength of the electrostatic interactions plays a peculiar role in the adsorption phenomenon.[38]

3.6.1. Global Chemical Reactivity. Molecular simulations have proven to be a very useful method to verify experimental results as well as to expand the investigations of clay and adsorbant properties to the extent that they are not experimentally feasible. The experimental findings by the theoretical Density functional theory (DFT) computations were used. The distribution of the electron density HOMO and LUMO orbitals, the total densities of the HOMO and LUMO, and the electrostatic potential map of the MB at the B3LYP/6-311+G(d,p) level of theory in aqueous solution using PCM solvation model are shown in Figure 18. It can be seen from the HOMO and LUMO surfaces that both HOMO and LUMO surfaces are widely spread on the whole moiety of the MB dye. This finding indicates that the investigated dye has a high electron-attracting capacity, suggesting its cationic nature. This is also confirmed by visualizing the total density of the HOMO and LUMO isosurfaces as well as the ESP map. The blue color of the ESP map reflects the cationic nature of the dye.[39] The relatively small value of the computed energy gap of the MB dye (2.422 eV)[40] signifies the strong interaction between the HOMO and LUMO and a high reactivity of the MB dye. The negative sign of the ΔE_{b-d} (Table 9), which considers the interaction of the tested dye with the clay surface, reflects that this cationic dye is expediently likely to accept electrons.[41]

3.7. Local Reactivity Indices. *3.7.1. Fukui Indices.* Importantly, the identification of the local active electrophilic and nucleophilic centers of the MB is very important in order to suggest a possible adsorption mechanism. To achieve this goal, two different indices, which are Fukui indices (FI) and Parr functions (PF),[42] were calculated. For this purpose, NBO analysis at the same level of theory for MB was performed.[43] The condensed Fukui indices for nucleophilic and electrophilic were performed by assessing entire natural bonding orbitals and natural population analysis for both inhibitors in their neutral (N), cationic $(N-1)$, and anionic $(N+1)$ radicals. The condensed Fukui functions for nucleophilic $((f_k^+)$, electrophilic $((f_k^-)$ attacks, as well as the condensed dual descriptors (f_k^2) were calculated by using the following equations:[44]

Nucleophilic attack: $f_k^{+q(N)-q(N+1)}$

Electrophilic attacks: $f_k^{-q(N-1)-q(N)}$

and

Dual Fukui function: $f_k^2 = q(N+1) - q(N-1)$

Table 5. Kinetic of the Various Parameters Using the MB Adsorption Dye at Different Concentrations

[MB] mg L^{-1}	10	20	40	60	80	100	200
Q_e mg g^{-1}	$10^{12.75}$	$10^{23.62}$	$10^{29.75}$	$10^{44.18}$	$10^{46.8535}$	$10^{52.01}$	$10^{80.6}$
K_1	0.232	0.405	0.500	0.740	0.797	0.875	1.318
R^2	0.79	0.41	0.25	0.42	0.39	0.47	0.63

Table 6. Kinetic Parameters Present the Organic MB Adsorption Dye at Various Concentrations

[MB] mg L^{-1}	10	20	40	60	80	100	200
Q_e mg g^{-1}	45.02	52.11	77.28	97.47	107.18	110.13	145.77
K_2	0.0653	0.0037	0.0357	0.0016	0.0018	0.0013	0.0006
R^2	1.00	0.998	0.996	0.996	0.997	0.995	0.990
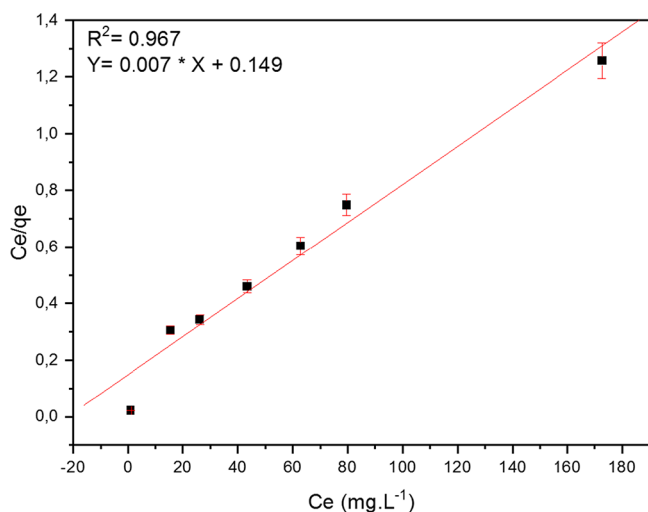
Figure 13. Linear transforms of the Langmuir adsorption isotherms.

Figure 14. Evolution of the different values of the separation factors with the concentration of the MB dye.

Figure 15. Linear transforms of Freundlich adsorption isotherms.

Table 7. Constant of the Langmuir and Freundlich Isotherms of Adsorption of MB on Clay

Langmuir	K_L	0.045
	Q_m	148.81
	R^2	0.967
Freundlich	K_F	38.76
	N	4.46
	R^2	0.803
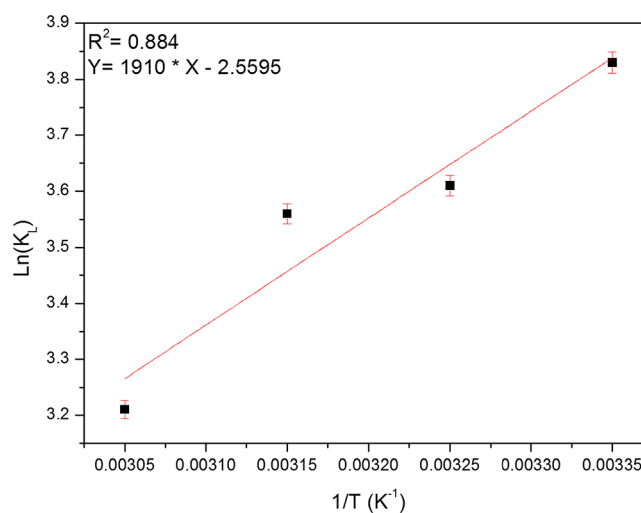
Figure 16. Van't Hoff curve of adsorption of organic dye MB on clay.

where $q(N)$, $q(N + 1)$, and $q(N - 1)$ are the Hirshfeld charges of the N, $N + 1$, and $N - 1$ systems, respectively. The Fukui functions and their condensed values were also visualized and calculated using the Multiwfn program.[45] The results of the condensed Fukui descriptors are summarized in Table 10. The distribution of the condensed Fukui functions $\left(f_k^{-,f_k^{+,\wedge}f_k^2}\right)$ indices and the 3D-isosurfaces of the Fukui functions are shown in Figure 19.

The results in Table 10 and Figure 19a indicate that the most reactive centers that are responsible for electrophilic attacks are N2=N3 > C7=C8 > S1 > C15=C16 > C11=C12. Whereas, the most reactive centers that are responsible for nucleophilic attacks are S1 > N4 > C13=C14 > C9=C10 > C5=C6. More accurate results are also obtained by considering the dual Fukui index, which reflects that the

centers with $f_k^2 < 0$ are more reliable for nucleophilic attacks (N2, N4, C7, and C8), while those centers with $f_k^2 > 0$ are responsible for electrophilic attacks (N4 > S1 > C5 > C6). These results are also confirmed when the 3D-isosurfaces of the nucleophilic and electrophilic Fukui functions and the distribution of the Mulliken charges are depicted (Figure 19c).

Table 8. Thermodynamics Parameters

T (K)	$1/T$ (K^{-1})	Ln (K_L)	Q_e (mg g^{-1})	C_e (mg L^{-1})	$\Delta G°$ (kJ mol^{-1})	$\Delta H°$ (kJ mol^{-1})	$\Delta S°$ (J mol^{-1} K^{-1})
298	0.00335	3.83	45	0.986	−6.23	−3.25	10.39
308	0.00324	3.61	43.98	1.19	−6.33		
318	0.00314	3.56	43.73	1.24	−6.43		
328	0.00304	3.21	41.58	1.67	−6.53		
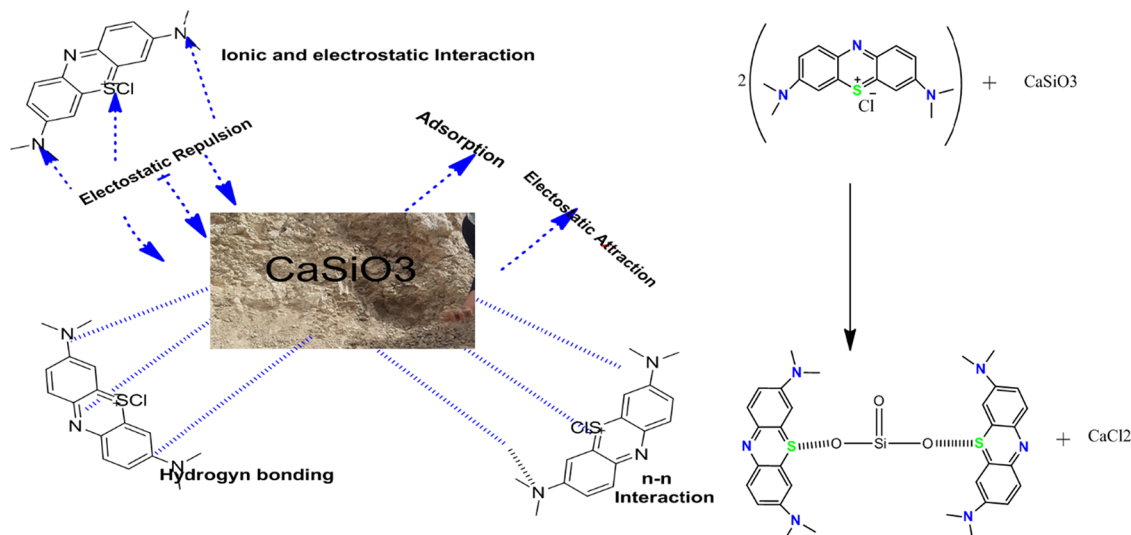
Figure 17. Mechanisms of the Ionic and Electrostatic Interaction of MB dye on the clay adsorbent.
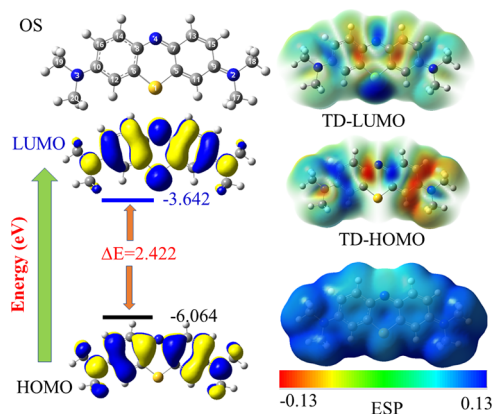
Figure 18. Optimized structure (OS), HOMO, LUMO, total density map at HOMO and LUMO (TD-HOMO and TD-LUMO), and molecular electrostatic potential map of the MB at the B3LYP/6-311+G(d,p) level of theory in aqueous solution using the PCM solvation model.

Table 9. Quantum Chemical Parameters of MB as Computed at the B3LYP/6-311+G(d,p) Level of Theory in Aqueous Solution Using the PCM Solvation Model

		MB
total energy	E_0	−32192.3984
energy of anion at geometries of neutral species (eV)	E_0^-	−32196.2250
energy of cation at geometries of neutral species (eV)	E_0^+	−32186.5322
energy of highest occupied molecular orbital (eV)	E_H	−6.065
energy of lowest occupied molecular orbital (eV)	E_L	−3.642
energy gap (eV)	ΔE	2.422
vertical ionization potential (eV)	IP_V	5.866
vertical electron affinity (eV)	EA_V	3.827
electronegativity (eV)	χ	4.846
hardness (eV)	η	2.040
softness (eV^{-1})	S	0.490
electrophilicity (eV)	ω	5.758
nucleophilicity (eV)	N	3.009
the back-donation energy	ΔE_{b-d}	−0.501
dipole moment (debye)	μ	3.27

3.7.2. Parr Functions. The local electrophilicity (ω_k) and the local nucleophilicity (N_k) concentrated on atom k were calculated based on global properties and the Parr function (P_k^+ or P_k^-), according to the formulas[46]

$$\omega_k = P_k^{+.\omega} \text{ and } N_k = P_k^{+.N}$$

The Parr functions (P_k^+ and P_k^-) were obtained, respectively, by Mulliken analysis of the atomic spin density (ASD) of the electrophilic and the nucleophile chemicals species by applying the NBO analysis.[47] Thus, it is easy to find the maximum values of ω_k and N_k, which correspond to the most electrophilic and most nucleophilic centers in a molecule, respectively. In addition, these maxima also correspond to the

centers with the highest electron density developed during the charge transfer process.

The results of Parr functions (electrophilic (ω_k) and nucleophilic (N_k)) of the MB system are summarized in Table 10. The distribution of these descriptors is also depicted in Figure 19b. The data in Table 10 and Figure 19b indicate that the calculated Parr functions are, to a large extent, in good agreement with the results of the LUMO electron densities and, to a small extent, with the Fukui indices. The Parr function results show that the maximum values of N_k are located at the N2(N3), C8(C7), and C15(C16) centers, which

Table 10. Electrophilic f_k^- and Nucleophilic f_k^+ Fukui Attacks Centers, Atomic Spin Densities (ASD) of Electrophile (P_k^+) and Nucleophilic Radicals (P_k^-), Parr Function for Electrophilic (ω_k) and Nucleophilic (N_k) Centers of the Methylene Blue Computed at the B3LYP/6-311+G(d,p) Level of Theory in Aqueous Solution Using the PCM Solvation Model

| atom	f_k^+	f_k^-	f_k^2	P_k^+	ω_k	P_k^-	N_k
S1	0.115	0.047	0.069	−0.048	−0.279	0.087	0.261
N2	0.036	0.070	-0.033	0.315	1.813	0.070	0.212
N3	0.036	0.070	-0.033	0.315	1.813	0.070	0.212
N4	0.094	0.022	0.072	−0.143	−0.825	0.363	1.093
C5	0.037	0.017	0.021	−0.095	−0.548	0.171	0.516
C6	0.037	0.017	0.021	−0.095	−0.548	0.171	0.516
C7	0.035	0.054	−0.020	0.216	1.243	−0.059	−0.177
C8	0.035	0.054	−0.020	0.216	1.243	−0.059	−0.177
C9	0.040	0.025	0.015	−0.068	−0.392	0.121	0.365
C10	0.040	0.025	0.015	−0.068	−0.392	0.121	0.365
C11	0.025	0.042	−0.017	0.144	0.826	−0.092	−0.278
C12	0.025	0.042	−0.017	0.144	0.826	−0.092	−0.278
C13	0.042	0.025	0.017	−0.107	−0.618	0.088	0.265
C14	0.042	0.025	0.017	−0.107	−0.618	0.088	0.265
C15	0.035	0.044	−0.009	0.160	0.920	−0.036	−0.109
C16	0.035	0.044	−0.009	0.160	0.920	−0.036	−0.109
C17	0.011	0.017	−0.006	0.016	0.094	0.005	0.017
C18	0.011	0.017	−0.006	0.016	0.091	0.006	0.017
C19	0.011	0.017	−0.006	0.016	0.091	0.006	0.017
C20	0.011	0.017	−0.006	0.016	0.094	0.005	0.017
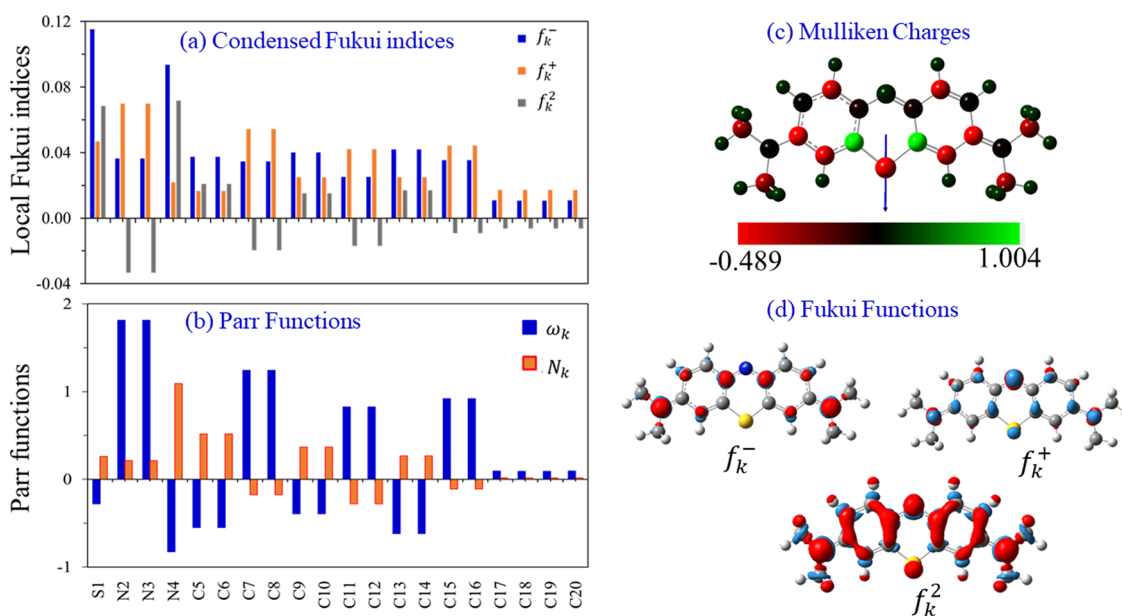
Figure 19. (a) Distribution of the local condensed Fukui functions for electrophilic (f_k^-) (blue), nucleophilic (f_k^+) (red), and dual attacks (f_k^2) (dark gray), (b) distribution of the Parr functions for electrophilicity (ω_k) and nucleophilicity (N_k), (c) distribution of the Mulliken charges, and (d) 3D-isosurfaces (Density = 0.003 au.) of the Fukui functions for nucleophilic, electrophilic, and dual Fukui functions ($f \mid k^2$). Red color corresponds to negative regions and the faint blue color corresponds to positive regions.

may be the preferred sites for electrophilic interactions. On the other hand, the N4, C5 (C6), and C9 (C10) have the highest N_k value, which reflects their tendency for nucleophilic attacks during the adsorption process.

3.8. Monte Carlo and Molecular Dynamic. In order to precisely determine the diverse energy outputs, it becomes imperative to ascertain the optimal adsorption configuration of the MB molecule, leading to the most efficient adsorption process. The interaction between the adsorbate molecule and the clay interface, represented by the SiO$_2$ and calcite models, serves as a valuable source of information. Analyzing this

interaction enables the calculation of adsorption energies associated with this methodology, thereby providing crucial insights into the energetics and stability of the system. Understanding the adsorption energies helps unravel the underlying mechanisms and aids in the design of effective adsorption strategies for MB and similar molecules on clay surfaces[48] (Figure 20). This can be done quantitatively by solving the following equation to derive the adsorption energy (E_{ads}) (eq 14):

$$E_{adsorption} = E_{MB \lor Adsorbent} - (E_{MB} + E_{Adsorbent}) \qquad (14)$$
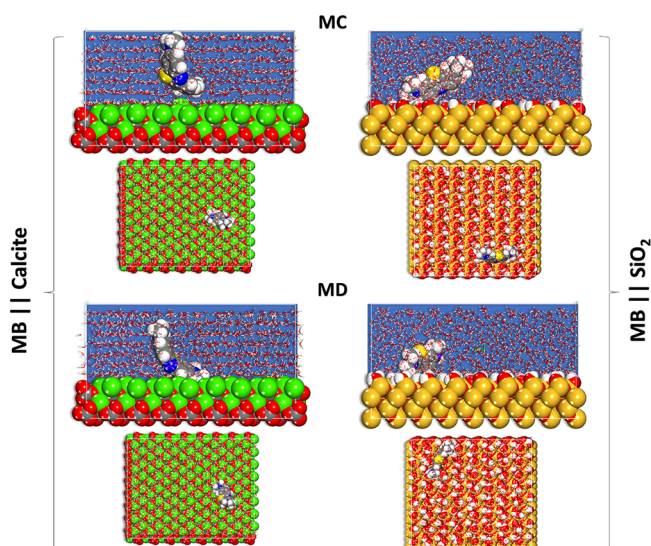
Figure 20. Lowest energy geometries derived from MC and MD for the MB molecule adsorbed onto interface SiO$_2$ and calcite.

where $E_{\text{MB} \vee \text{Adsorbent}}$ is the total energy of the interacting surface and entities, E_{MB}, and $E_{\text{Adsorbent}}$ is the total energy of the entities.

The MC approach employed to assess molecular complexity involves the generation of numerous combinations of simulation-relevant species such as molecules and ions. These combinations are randomly generated, allowing for a comprehensive exploration of various configurations.[49] The adsorption geometries of the adsorbate molecules are depicted in Figure 20, highlighting their proximity to the SiO$_2$ and calcite interfaces. This proximity leads to robust interactions, resulting in negative adsorption energies of considerable magnitude, as illustrated in Figure 21.[49] The observed strong
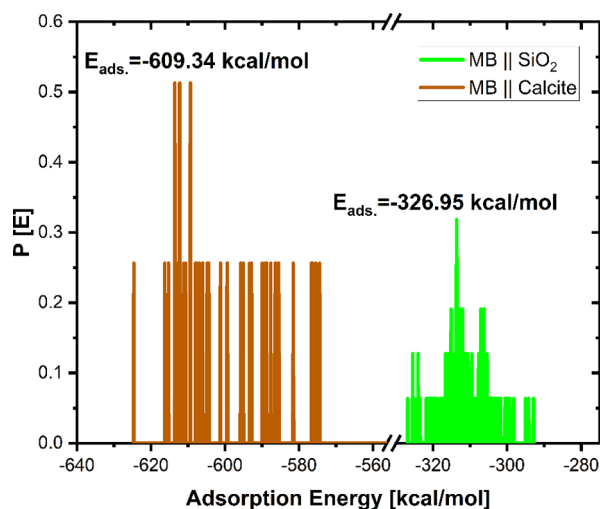
Figure 21. Probability distribution of the adsorption energies from MC for the MB molecule onto interface SiO$_2$ and calcite.

interactions and high negative adsorption energies signify the affinity and stability of the MB molecules at the interface. These findings offer valuable insights into the adsorption behavior and shed light on the intricate dynamics of interactions of MB with the SiO$_2$ and calcite surfaces.

The experimental results are corroborated by the note-worthy observation that the adsorbate molecules adsorbed on the surface of SiO$_2$ and calcite displayed a significantly higher magnitude of negative adsorption energy (E_{ads}). The enhanced negative Eads values highlight the robust binding and favorable adsorption characteristics of the adsorbate molecules on the adsorbent surfaces.[50] This information supports the understanding that the adsorbent provides an ideal substrate for effective adsorption, potentially leading to improved adsorption capacities and enhanced performance in relevant applications.[51] The MD simulation was meticulously executed, with minimal temperature drift observed (Figure 22), ensuring a stable and reliable run.
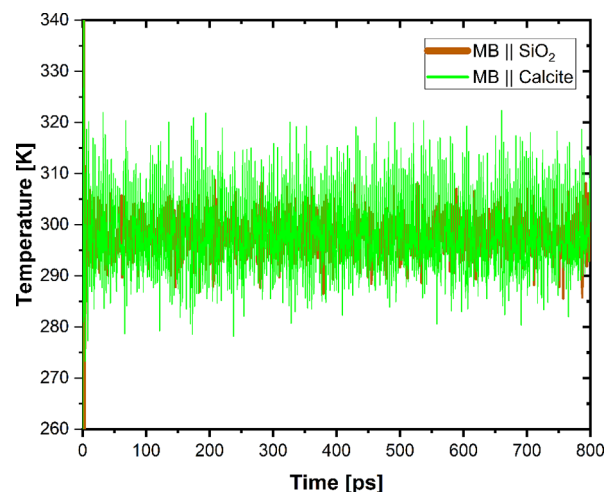

Figure 22. Temperature fluctuations during the MD run for the MB molecule adsorption onto the surface of SiO$_2$ and calcite.

The controlled temperature conditions facilitated an accurate analysis of the molecular dynamics and interactions. The minimal temperature drift validates the simulation's robustness, confirming the suitability of parameters and enhancing confidence in the obtained data.[52] These findings yield a comprehensive understanding of the system's behavior and properties under simulated conditions.[53]

Furthermore, the computation of the relative MB concentration (Figure 23) on the respective surfaces further supports the findings. The analysis demonstrates that MB molecules exhibit a strong affinity for the surfaces, adhering effectively. This alignment between the computational results and experimental observations re-inforces the validity and reliability of the simulations. The successful adhesion of MB molecules to the surfaces provides a solid foundation for the experimental findings, establishing a coherent and congruent understanding of the MB-surface interactions.

These results contribute to the overall confidence in the accuracy of the simulation outcomes and highlight the potential of computational approaches in complementing and supporting experimental investigations in the field of MB adsorption.[54]

4. CONCLUSIONS

The results obtained by using clay for MB adsorption from aqueous solutions were studied.
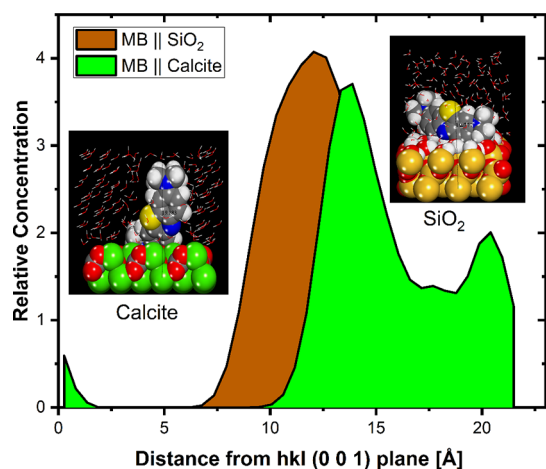
Figure 23. Relative concentration of the MB during the MD run onto the surface of SiO$_2$ and calcite.

techniques for MB and similar compounds on clay surfaces. The MC technique allows for a thorough examination of configurations by creating many simulation-relevant species combinations, while the observed strong contacts and large negative adsorption energies show the affinity and stability of MB molecules at the interface. The experimental findings, which are confirmed by a computational examination of the relative MB concentration and temperature drift during MD simulations, validate the robustness and reliability of the simulation results, increasing confidence in their accuracy. This integrated approach highlights the utility of computational tools in supplementing the experimental studies of MB adsorption.

■ AUTHOR INFORMATION

Corresponding Authors

Jaouad Bensalah − *Laboratory of Advanced Materials and Process Engineering (LAMPE), Department of Chemistry, Faculty of Sciences, Ibn Tofaïl University, 14000 Kenitra, Morocco; Chemistry platform, UATRS, National Center for Scientific and Technical Research (CNRST), 10500 Rabat, Morocco*; Email: Jaouad.bensalah@uit.ac.ma

Musaab Dauelbait − *Department of Scientific translation, Faculty of Translation, University of Bahri, Bahri 11111, Sudan;* ⊙ orcid.org/0009-0003-0685-8243; Email: musaabelnaim@gmail.com

Authors

Zineb El Kerdoudi − *Laboratory of Organic Chemistry, Catalysis, and Environment(LOCCE), Department of Chemistry, Faculty of Sciences, Ibn Tofaïl University, 14000 Kenitra, Morocco*

Nouhaila Ferraa − *Laboratory of Organic Chemistry, Catalysis, and Environment(LOCCE), Department of Chemistry, Faculty of Sciences, Ibn Tofaïl University, 14000 Kenitra, Morocco*

Abdelali El Mekkaoui − *Laboratory of Organic Chemistry, Catalysis, and Environment(LOCCE), Department of Chemistry, Faculty of Sciences, Ibn Tofaïl University, 14000 Kenitra, Morocco*

Avni Berisha − *Department of Chemistry, Faculty of Natural and Mathematics Science, University of Prishtina, 10000 Prishtina, Kosovo*

Zaki Safi − *Department of Chemistry, Faculty of Science, Al-Azhar University of Gaza, Gaza 01277, Palestine*

Hanae Ouaddari − *Laboratory of Advanced Materials and Process Engineering (LAMPE), Department of Chemistry, Faculty of Sciences, Ibn Tofaïl University, 14000 Kenitra, Morocco; Chemistry platform, UATRS, National Center for Scientific and Technical Research (CNRST), 10500 Rabat, Morocco*

Farid Khallouki − *Biology Department, FSTE, University Moulay Ismail, 52000 Errachidia, Morocco*

Hiba-Allah Nafidi − *Department of Food Science, Faculty of Agricultural and Food Sciences, Laval University, Quebec City, QC G1 V 0A6, Canada*

Abdel-Rhman Z. Gaafar − *Department of Botany and Microbiology, College of Science, King Saud University, Riyadh 11451, Saudi Arabia*

Mohammed Bourhia − *Department of Chemistry and Biochemistry, Faculty of Medicine and Pharmacy, Ibn Zohr University, Laayoune 70000, Morocco*

The micrographs of the clay showed different surface magnifications of the clay raw material, indicating a favorable multiphase structure for the adsorbents.

The EDX spectrum obtained after the adsorption of the MB dye on the clay indicated a peak that represented the chlorine of the dye following the complex reaction. The examination of the diffraction diagram of the raw clay shows the presence of intense lines that characterize calcite, quartz, rutile syn, and magnetite. FX results indicated the presence of calcium silicates (CaSiO3). Adsorption equilibrium was achieved in 180 min with a small quantity of clay such as 0.02 g and at a pH of 6.5.

Therefore, the negative value of (ΔH^0) and the positive value of (ΔS^0) showed that the exothermic nature of the adsorption of MB on the clay is confirmed, and the order of distribution of the dye molecules on the adsorbent increases compared to that of the solution, respectively. Negative (ΔG^0) values indicated that the adsorption process is spontaneous. The adsorption capacity changes from 45 to 147.2 mg g^{-1} for MB concentration of 10−200 mg L^{-1} respectively. The adsorption kinetics of MB study the pseudo second order model. From the results of the R_L values for the current clay, it was concluded that the clay is an effective adsorbent for the cationic dye MB. The Langmuir isotherm has a higher R^2 correlation than the Freundlich isotherm for our clay; this means that the Langmuir isotherm describes the adsorption much better than the Freundlich isotherm.

The DFT analysis confirmed that the energy gap of the methylene blue dye is relatively small, indicating its high chemical reactivity. Our results concluded that the electrophilic attacks take place at the two terminal nitrogen atoms (N2 and N3), while the nucleophilic attacks take place at central nitrogen atom (N4) and the adjacent β-carbon atoms (C5 and C6)

Ultimately, identifying the best adsorption configuration of the MB molecule is critical for precisely calculating various energy outputs and achieving an efficient adsorption process. The interaction between the adsorbate molecule and the clay interface, as represented by SiO$_2$ and calcite models, gives useful information for assessing and computing adsorption energies, revealing system energetics and stability. These findings contribute to the understanding of underlying mechanisms and the development of appropriate adsorption

Amar Habsaoui − *Laboratory of Organic Chemistry, Catalysis, and Environment(LOCCE), Department of Chemistry, Faculty of Sciences, Ibn Tofaïl University, 14000 Kenitra, Morocco*

Nouredine EL Mejdoub − *Laboratory of Organic Chemistry, Catalysis, and Environment(LOCCE), Department of Chemistry, Faculty of Sciences, Ibn Tofaïl University, 14000 Kenitra, Morocco*

Complete contact information is available at:
https://pubs.acs.org/10.1021/acsomega.3c06019

Notes
The authors declare no competing financial interest.

■ REFERENCES

(1) Zhang, W.; Yan, H.; Li, H.; Jiang, Z.; Dong, L.; Kan, X.; Yang, H.; Li, A.; Cheng, R. Removal of dyes from aqueous solutions by straw based adsorbents: Batch and column studies. *Chem. Eng. J.* **2011**, *168*, 1120−1127.

(2) Yang, S.; Li, J.; Shao, D.; Hu, J.; Wang, X. Adsorption of Ni(II) on oxidized multi-walled carbon nanotubes: Effect of contact time, pH, foreign ions and PAA. *J. Hazard. Mater.* **2009**, *166*, 109−116.

(3) Wahi, R. K.; Yu, W. W.; Liu, Y.; Mejia, M. L.; Falkner, J. C.; Nolte, W.; Colvin, V. L. Photodegradation of Congo Red catalyzed by nanosized TiO2. *J. Mol. Catal. Chem.* **2005**, *242*, 48−56.

(4) Yin, J.; Zhan, F.; Jiao, T.; Deng, H.; Zou, G.; Bai, Z.; Zhang, Q.; Peng, Q. Highly efficient catalytic performances of nitro compounds via hierarchical PdNPs-loaded MXene/polymer nanocomposites synthesized through electrospinning strategy for wastewater treatment. *Chin. Chem. Lett.* **2020**, *31*, 992−995.

(5) Tahir, H.; Sultan, M.; Akhtar, N.; Hameed, U.; Abid, T. Application of natural and modified sugar cane bagasse for the removal of dye from aqueous solution. *J. Saudi Chem. Soc.* **2016**, *20*, S115−S121.

(6) Yin, J.; Zhan, F.; Jiao, T.; Wang, W.; Zhang, G.; Jiao, J.; Jiang, G.; Zhang, Q.; Gu, J.; Peng, Q. Facile preparation of self-assembled MXene@Au@CdS nanocomposite with enhanced photocatalytic hydrogen production activity. *Sci. China Mater.* **2020**, *63*, 2228−2238.

(7) Mallakpour, S.; Tabesh, F. Tragacanth gum based hydrogel nanocomposites for the adsorption of methylene blue: Comparison of linear and non-linear forms of different adsorption isotherm and kinetics models. *Int. J. Biol. Macromol.* **2019**, *133*, 754−766.

(8) Lee, C.; Yoon, J. Temperature dependence of hydroxyl radical formation in the hv/Fe3+/H2O2 and Fe3+/H2O2 systems. *Chemosphere* **2004**, *56*, 923−934.

(9) Lan, Y.-C.; Kamal, S.; Lin, C.-C.; Liu, Y.-H.; Lu, K.-L. Ultra-thin Zr-MOF/PVA/Melamine composites with remarkable sound attenuation effects. *Microporous Mesoporous Mater.* **2023**, *360*, No. 112668.

(10) Kuki, Á.; Nagy, L.; Zsuga, M.; Kéki, S. Fast identification of phthalic acid esters in poly(vinyl chloride) samples by Direct Analysis In Real Time (DART) tandem mass spectrometry. *Int. J. Mass Spectrom.* **2011**, *303*, 225−228.

(11) Hameed, B. H.; Ahmad, A. A. Batch adsorption of methylene blue from aqueous solution by garlic peel, an agricultural waste biomass. *J. Hazard. Mater.* **2009**, *164*, 870−875.

(12) Giovannoli, C.; Passini, C.; Volpi, G.; Di Nardo, F.; Anfossi, L.; Baggiani, C. Peptide-based affinity media for solid-phase extraction of Ochratoxin A from wine samples: Effect of the solid support on binding properties. *Talanta* **2015**, *144*, 496−501.

(13) Gackowski, M.; Tarach, K.; Kuterasiński, Ł.; Podobiński, J.; Sulikowski, B.; Datka, J. Spectroscopic IR and NMR studies of hierarchical zeolites obtained by desilication of zeolite Y: Optimization of the desilication route. *Microporous Mesoporous Mater.* **2019**, *281*, 134−141.

(14) Gackowski, M.; Tarach, K.; Kuterasiński, Ł.; Podobiński, J.; Jarczewski, S.; Kuśtrowski, P.; Datka, J. Hierarchical zeolites Y obtained by desilication: Porosity, acidity and catalytic properties. *Microporous Mesoporous Mater.* **2018**, *263*, 282−288.

(15) Elabboudi, M.; Bensalah, J.; Amri, A. E.; Azzouzi, N. E.; Srhir, B.; Lebkiri, A.; Zarrouk, A.; Rifi, E. H. Adsorption performance and mechanism of anionic MO dye by the adsorbent polymeric Amberlite®IRA-410 resin from environment wastewater: Equilibrium kinetic and thermodynamic studies. *J. Mol. Struct.* **2023**, *1277*, No. 134789.

(16) El Kerdoudi, Z.; Bensalah, J.; Helli, H.; El Mekkaoui, A.; El Mejdoub, N. Investigation of the cationic dye methylene blue in the treatment of wastewater clay from Sidi-Kacem (Morocco): Kinetic and mathematical modelling of experimental data. *Mater. Today Proc.* **2023**, *72*, 3550−3555.

(17) Spoor, W.; Zohary, D; Hopf, M. *Domestication of plants in the Old World*, 3rd edition; Oxford University Press: New York, 2000, 316 pp.

(18) Ylmén, R.; Jäglid, U.; Steenari, B.-M.; Panas, I. Early hydration and setting of Portland cement monitored by IR, SEM and Vicat techniques. *Cem. Concr. Res.* **2009**, *39*, 433−439.

(19) Yang, S.; Li, J.; Shao, D.; Hu, J.; Wang, X. Adsorption of Ni(II) on oxidized multi-walled carbon nanotubes: Effect of contact time, pH, foreign ions and PAA. *J. Hazard. Mater.* **2009**, *166*, 109−116.

(20) Bensalah, J.; Berradi, M.; Habsaoui, A.; Allaoui, M.; Essebaai, H.; El Khattabi, O.; Lebkiri, A.; Rifi, E.-H. Kinetic and thermodynamic study of the adsorption of cationic dyes by the cationic artificial resin Amberlite®IRC50. *Mater. Today Proc.* **2021**, *45*, 7468−7472.

(21) Dasari, M. A.; Kiatsimkul, P.-P.; Sutterlin, W. R.; Suppes, G. J. Low-pressure hydrogenolysis of glycerol to propylene glycol. *Appl. Catal. Gen.* **2005**, *281*, 225−231.

(22) Dahmani, K.; Galai, M.; Elhasnaoui, A.; Temmar, B.; Hessni, A.E.; Cherkaoui, M. Corrosion resistance of electrochemical copper coating realized in the presence of essential oils. *Der Pharma Chem.* **2015**, *7*, 566.

(23) Climent, M. J.; Corma, A.; De Frutos, P.; Iborra, S.; Noy, M.; Velty, A.; Concepción, P. Chemicals from biomass: Synthesis of glycerol carbonate by transesterification and carbonylation with urea with hydrotalcite catalysts. The role of acid−base pairs. *J. Catal.* **2010**, *269*, 140−149.

(24) Amri, A. E.; Bensalah, J.; Idrissi, A.; Lamya, K.; Ouass, A.; Bouzakraoui, S.; Zarrouk, A.; Rifi, E. H.; Lebkiri, A. Adsorption of a cationic dye (Methylene bleu) by Typha Latifolia: Equilibrium, kinetic, thermodynamic and DFT calculations. *Chem. Data Collect.* **2022**, *38*, No. 100834.

(25) Basavarao, V.; Rammohanrao, S. Adsorption studies on treatment of textile dyeing industrial effluent by flyash. *Chem. Eng. J.* **2006**, *116*, 77−84.

(26) Bensalah, J.; Habsaoui, A.; Abbou, B.; Kadiri, L.; Lebkiri, I.; Lebkiri, A.; Rifi, E. H. Adsorption of the anionic dye methyl orange on used artificial zeolites: kinetic study and modeling of experimental data. *Mediterr. J. Chem.* **2019**, *9*, 311−316.

(27) Bensalah, J.; Galai, M.; Ouakki, M.; Amri, A. E.; Hanane, B.; Habsaoui, A.; Khattabi, O. E.; Lebkiri, A.; Zarrouk, A.; Rifi, E. H. A combined experimental and thermodynamics study of mild steel corrosion inhibition in 1.0 M hydrochloric solution by the cationic

polymer Amberlite®IRC-50 resin extract. *Chem. Data Collect.* **2023**, *43*, No. 100976.

(28) Bensalah, J.; Berradi, M.; Habsaoui, A.; Dagdag, O.; Amri, A.E.; Khattabi, O.E.; Lebkiri, A.; Rifi, E.H.; Adsorption of the orange methyl dye and lead (II) by the cationic resin Amberlite®IRC-50: Kinetic study and modeling of experimental data, *J. Chem. Soc. Pak.* 2021 43 535.

(29) Bensalah, J.; Benhiba, F.; Habsaoui, A.; Ouass, A.; Zarrouk, A.; Lebkiri, A.; El Khattabi, O.; Rifi, E. H. The adsorption mechanism of the anionic and cationic dyes of the cationic resin A®IRC-50, kinetic study and theoretical investigation using DFT. *J. Indian Chem. Soc.* **2022**, *99*, No. 100512.

(30) Badri, N.; Zbair, M.; Sahibed-Dine, A.; Chhiti, Y.; Khamliche, L.; Bensitel, M. Adsorption of Cationic Dyes by Waste Biomass Treated by Phosphoric Acid. *J. Mater. Environ. Sci.* **2018**, *9*, 1636 DOI: 10.26872/jmes.2018.9.6.182.

(31) Aresta, M.; Dibenedetto, A.; Nocito, F.; Ferragina, C. Valorization of bio-glycerol: New catalytic materials for the synthesis of glycerol carbonate via glycerolysis of urea. *J. Catal.* **2009**, *268*, 106−114.

(32) An, X.; Gao, C.; Liao, J.; Wu, X.; Xie, X. Synthesis of mesoporous N-doped TiO_2/ZnAl-layered double oxides nano-composite for efficient photodegradation of methyl orange. *Mater. Sci. Semicond. Process.* **2015**, *34*, 162−169.

(33) Amri, A. E.; Bensalah, J.; Essaadaoui, Y.; Lebkiri, I.; Abbou, B.; Zarrouk, A.; Rifi, E. H.; Lebkiri, A. Elaboration, characterization and performance evaluation of a new environmentally friendly adsorbent material based on the reed filter (Typha Latifolia): Kinetic and thermodynamic studies and application in the adsorption of Cd (II) ion. *Chem. Data Collect.* **2022**, *39*, No. 100849.

(34) Bensalah, J.; Amri, A. E.; Ouass, A.; Hammani, O.; Kadiri, L.; Ouaddari, H.; Mustapha, S. E.; Zarrouk, A.; Lebkiri, A.; Srhir, B.; Rifi, E. H. Investigation of the cationic resin Am®IRC-50 as a potential adsorbent of Co (II): Equilibrium isotherms and thermodynamic studies. *Chem. Data Collect.* **2022**, *39*, No. 100879.

(35) Zhao, D.; Sheng, G.; Hu, J.; Chen, C.; Wang, X. The adsorption of Pb(II) on Mg2Al layered double hydroxide. *Chem. Eng. J.* **2011**, *171*, 167−174.

(36) Visconti, C. G.; Lietti, L.; Tronconi, E.; Forzatti, P.; Zennaro, R.; Finocchio, E. Fischer−Tropsch synthesis on a Co/Al2O3 catalyst with CO2 containing syngas. *Appl. Catal. Gen.* **2009**, *355*, 61−68.

(37) Sadowska, K.; Wach, A.; Olejniczak, Z.; Kuśtrowski, P.; Datka, J. Hierarchic zeolites: Zeolite ZSM-5 desilicated with NaOH and NaOH/tetrabutylamine hydroxide. *Microporous Mesoporous Mater.* **2013**, *167*, 82−88.

(38) Rahmat, N.; Abdullah, A. Z.; Mohamed, A. R. Recent progress on innovative and potential technologies for glycerol transformation into fuel additives: A critical review. *Renew. Sustainable Energy Rev.* **2010**, *14*, 987−1000.

(39) Zarrok, H.; Zarrouk, A.; Salghi, R.; Touhami, M. E.; Oudda, H.; Hammouti, B.; Touir, R.; Bentiss, F.; Al-Deyab, S. S. Corrosion Inhibition of C38 Steel in Acidic Medium Using N-1 Naphthylethy-lenediamine Dihydrochloride Monomethanolate. *Int. J. Electrochem Sci.* **2013**, *8*, 6014−6032.

(40) Yadav, D. K.; Quraishi, M. A.; Maiti, B. Inhibition effect of some benzylidenes on mild steel in 1 M HCl: An experimental and theoretical correlation. *Corros. Sci.* **2012**, *55*, 254−266.

(41) Tomasi, J.; Mennucci, B.; Cammi, R. Quantum Mechanical Continuum Solvation Models. *Chem. Rev.* **2005**, *105*, 2999−3094.

(42) Singh, R.; Prasad, D.; Safi, Z.; Wazzan, N.; Guo, L. De-scaling, experimental, DFT, and MD-simulation studies of unwanted growing plant as natural corrosion inhibitor for SS-410 in acid medium. *Colloids Surf. Physicochem. Eng. Asp.* **2022**, *649*, No. 129333.

(43) Singh, D. K.; Kumar, S.; Udayabhanu, G.; John, R. P. 4(N,N-dimethylamino) benzaldehyde nicotinic hydrazone as corrosion inhibitor for mild steel in 1 M HCl solution: An experimental and theoretical study. *J. Mol. Liq.* **2016**, *216*, 738−746.

(44) Sherif, E.-S. M.; Erasmus, R. M.; Comins, J. D. Inhibition of copper corrosion in acidic chloride pickling solutions by 5-(3-aminophenyl)-tetrazole as a corrosion inhibitor. *Corros. Sci.* **2008**, *50*, 3439−3445.

(45) Ramanathan, T.; Gurudeeban, S.; Satyavai, K. Antioxidant and Radical Scavenging Effect of Citrullus colocynthis. *Invent Rapid* 2010, 1.

(46) Raja, P. B.; Sethuraman, M. G. Natural products as corrosion inhibitor for metals in corrosive media — A review. *Mater. Lett.* **2008**, *62*, 113−116.

(47) Puschmann, H. 4th European symposium on corrosion inhibitors. (82. Veranstaltung der Europäischen Föderation Korrosion), Ferrara, 15. bis 19. September 1975. In *Proceedings, Mater. Corrosion*, 1975 pp. 992−992.

(48) Prasad, D.; Dagdag, O.; Safi, Z.; Wazzan, N.; Guo, L. Cinnamoum tamala leaves extract highly efficient corrosion bio-inhibitor for low carbon steel: Applying computational and experimental studies. *J. Mol. Liq.* **2022**, *347*, No. 118218.

(49) Martínez-Araya, J. I. Why is the dual descriptor a more accurate local reactivity descriptor than Fukui functions? *J. Math. Chem.* **2015**, *53*, 451−465.

(50) Nehdi, I. A.; Sbihi, H.; Tan, C. P.; Al-Resayes, S. I. Evaluation and characterisation of Citrullus colocynthis (L.) Schrad seed oil: Comparison with Helianthus annuus (sunflower) seed oil. *Food Chem.* **2013**, *136*, 348−353.

(51) Lu, T.; Chen, F. Multiwfn: A multifunctional wavefunction analyzer. *J. Comput. Chem.* **2012**, *33*, 580−592.

(52) Li, X.; Deng, S.; Fu, H. Triazolyl blue tetrazolium bromide as a novel corrosion inhibitor for steel in HCl and H2SO4 solutions. *Corros. Sci.* **2011**, *53*, 302−309.

(53) Kouadri, I.; Satha, H. Extraction and characterization of cellulose and cellulose nanofibers from Citrullus colocynthis seeds. *Ind. Crops Prod.* **2018**, *124*, 787−796.

(54) Asan, A.; Soylu, S.; Kıyak, T.; Yıldırım, F.; Öztaş, S. G.; Ancın, N.; Kabasakaloğlu, M. Investigation on some Schiff bases as corrosion inhibitors for mild steel. *Corros. Sci.* **2006**, *48*, 3933−3944.